A fractional rate-dependent cohesive-zone model

Marco Musto[*,†] and Giulio Alfano

Department of Mechanical, Aerospace and Civil Engineering, Brunel University, Kingston Lane, UB8 3PH, Uxbridge, UK

SUMMARY

This paper presents a novel formulation of a hereditary cohesive zone model able to effectively capture rate-dependent crack propagation along a defined interface, over a wide range of applied loading rates and with a single set of seven input parameters only, as testified by the remarkable agreement with experimental results in the case of a double cantilever beam made of steel adherends bonded along a rubber interface. The formulation relies on the assumption that the measured fracture energy is the sum of a rate-independent 'rupture' energy, related to the rupture of primary bonds at the atomic or molecular level, and of additional dissipation caused by other rate-dependent dissipative mechanisms present in the material and occurring simultaneously to rupture. The first contribution is accounted for by introducing a damage-type internal variable, whose evolution follows a rate-independent law for consistency with the assumption of rate independence of the rupture energy. To account for the additional dissipation, a fractional-calculus-based linear viscoelastic model is used, because for many polymers, it is known to capture the material response within an extremely wide range of strain rates much more effectively than classic models based on an exponential kernel. To the authors' knowledge, this is the first application of fractional viscoelasticity to the simulation of fracture. © 2015 The Authors. *International Journal for Numerical Methods in Engineering* published by John Wiley & Sons Ltd.

1. INTRODUCTION

Rate dependence of crack initiation and/or growth is an important and sometimes essential aspect to be taken into account in a wide class of applications, particularly in aerospace, automotive and biomedical engineering, see [1–4] among many others. Theoretically, the problem can be studied in the framework of the Griffith theory of fracture, by assuming that in the rate-dependent case, the fracture energy G_c, intended as the total energy dissipated per unit of new formed crack area, is a function of the crack speed $\dot{a}$, i.e., $G_c = \gamma(\dot{a})$. However, this typically leads to the determination of γ through phenomenological approaches, although in [5], an analytical derivation of γ from the material viscoelastic spectrum is presented, valid for a crack in an infinite body, see also [6, 7].

An alternative approach is represented by the use of cohesive-zone models (CZMs) that, in the authors' opinion, provide a framework in which it is easier to account for the underlying physical mechanisms causing rate dependence. It is also worth noting that, although in its classical implementation CZMs are used as constitutive law for interface elements, which requires *a priori* knowledge of the crack path, alternative approaches overcoming this limitation have been developed by implementing the cohesive-zone concept within the X-FEM (see [8, 9] among others) or, more recently, phase field modelling [10].

*Correspondence to: Marco Musto, Department of Mechanical, Aerospace and Civil Engineering, Brunel University, Kingston Lane, UB8 3PH, Uxbridge, UK.

†E-mail: musto.marco@outlook.com

Noting that the overall rate dependence can arise as a consequence of rate dependence of the bulk material's behaviour, of the interface response itself or of both, the attention here is restricted to models able to reproduce rate dependence at the interface level. Xu *et al.* [1, 11] constructed a rate-dependent CZM by adding the contributions from a rate-independent and a rate-dependent element, the latter given by a viscoelastic Maxwell element. The model quite satisfactorily replicates a class of experimental results and is characterised by the fact that, at a single point of the interface, the traction discontinuously goes to zero after reaching a threshold displacement given by a critical separation. Corigliano *et al.* [12] also focus on the rate dependence of the interface to model a (DCB) carbon-fibre-poly-ether-imide specimen. The interface deterioration is reproduced using two alternative phenomenological approaches, one of them based on softening plasticity and a second one in which a rate-dependent damage evolution law is adopted. Another example is the model proposed by Allen and Searcy [13], in which the CZM is conceived through a homogenisation procedure conducted at the micromechanical scale.

Liechti *et al.* [14] introduced rate-dependent behaviour in both the bulk material and the interface, motivating their decision by observing significant differences in the crack surface depending on test speed, which convinced them of the necessity of modelling the viscous losses at the interface. They also assumed the interface strength could be assimilated to a non-linear elastic response summed to a viscous contribution, given by a non-Newtonian dashpot. Damage evolution is implicit in their formulation as the elastic response is given by a bilinear traction-separation law. Furthermore, the authors suggest that the use of a non-Newtonian dashpot could possibly reproduce the rate-dependent nature of void formation. The model proposed by Hutchinson *et al.* [15] follows the same approach of introducing rate dependence in both the bulk and the interface. They are able to investigate the competing effects and present an explanation for the possible nonmonotonic relationship between crack speed and toughness. The rate dependence of the CZM is taken to obey a functional form similar to the elasto-viscoplastic formulation used to model the bulk material.

In general, the question whether it is necessary to account for rate dependence at the interface level at all could be considered open. Indeed, important results have been obtained, not considering the dissipation occurring at the interface, capturing the overall behaviour by simply focusing on the bulk material (as in the 'viscoelastic trumpet' approach of De Gennes, [16], see also [5, 17], as well as [18] for a numerical study). In our opinion, part of the answer depends on the physical meaning appended to the concept of 'interface'. While in general an interface could be considered as a surface in the geometric sense of the term, in the cohesive-zone approach herein followed, the interface is assigned a mechanical behaviour that indeed originates from the interaction of the crack with a process zone, which is possibly very thin, yet of finite thickness (see also the pertinent discussion in [19, 20] or the implementation of this concept within the X-FEM to account for the finite-thickness of the process zone [9]). This region of finite measure is 'lumped' into a line (or a surface in 3D), and hence, it seems to be necessary to account for its own time dependence. If this is necessary at all in general is a question which we do not attempt to answer, satisfied by the considerable computational advantages the present approach supplies; in many structures, elastic materials are bonded using polymers, and the analysis could be cheaply performed by avoiding modelling the polymeric layer altogether, under certain restrictions, replacing it with interface elements. It is also interesting to compare the aforementioned observation with the experimental work of Hauch and Marder [21]. They observed how the increase in fracture energy with crack speed was matched by the development of a microstructure of branching transversal cracks whose length and density was increasing too, a well-known aspect [22] which led to the development of phenomenological CZMs to capture crack-branching-related rate dependence at high speed, e.g., [23, 24]. Hauch and Marder also noted although that, below a certain speed, the fracture energy was still not constant in spite of the lack of any observable transversal crack pattern. Upon dissection of the specimens, it was found that the additional dissipation was likely to be connected with some 'subsurface activity' in their terminology. The authors wonder if these occurrences can only be accounted for by introducing the rate dependence at the interface level.

Based on the aforementioned considerations and focusing attention on problems involving pure mode-I crack propagation, in this paper, our aim is to capture the rate dependence within the process zone of the interface itself regardless of the behaviour of the surrounding material, resorting to first

principles. It is clear that assumptions will be necessary to model such a complex phenomenon as fracture, yet the intention is to develop a general, physically well-based CZM, without resorting to any phenomenological law other than basic physical and engineering understanding.

As a cornerstone of our modelling approach, we recognise the existence of an intrinsic, i.e., rate-independent, 'rupture' energy associated with an elastic energy threshold, in turn related to the energy of the bonds to be broken at the micro or possibly atomistic scale [25, 26]. We then use a damage-mechanics approach and introduce a suitably defined damage variable whose evolution is rate independent and is related to the difference between the energy threshold and the elastic energy. The rate dependence of the overall dissipated energy during crack propagation is a natural by-product of additional viscous dissipation introduced within the interface and of the effect that such viscous behaviour has on the specific elastic energy itself. In this way, no *ad hoc* phenomenon is invoked to explain the additional dissipation other than the dissipative mechanisms inherent to the material.

It is then postulated that a reasonable characterisation of the interface rate dependence can be achieved by assuming that the interfaces behaves, in a suitably defined way, as its constituent material considered as a continuum, while the variables of the model are suitably adapted. This is a result of the dimension reduction implied by the use of a CZM, whereby displacement jumps at the interface replace continuum strains as new deformation measures. On the other hand, the most complicated nonlinear processes occur within the process zone [27], and they are likely to be only partially probed during the material characterisation conducted on the bulk material. Hence, in this work, we are not stretching this dimensional-reduction approach to the point of assuming that the input parameters of the model can be determined from the material properties of the interface material considered as a continuum. While this ambitious aim may be considered for future developments of this research, in the current setting, we still rely on numerical calibration for the determination of the input parameters of the model.

Motivated by our aim of applying the formulation to rubber interfaces, a fractional-calculus-based linear viscoelastic model is used to characterise the continuum-like behaviour of the interface material. This is because, for many polymers and for rubber in particular, fractional viscoelasticity is known to capture the material response within a wide range of strain rates much more effectively than classic models based on exponential relaxation functions. This entails a significant enhancement with respect to earlier work [28], where an exponential kernel with one relaxation time was used.

The main advantage of fractional formulations is the ability to predict the viscoelastic response with many less constants than what is required using exponential kernels. Another very relevant advantage is the possibility to attempt an extrapolation outside the range of rates used for the calibration of the material constants, which is a result of the better physical foundation of fractional viscoelastic models compared to exponential ones. Instead, for the latter, the validity of the calibration exercise is restricted to the range over which such calibration is performed. This can be also explained considering that fractional models are related to a relaxation function displaying a power-law decay: such characteristic is outside the reach of exponential models, whose decay for times sufficiently larger than the largest relaxation time is exponential by definition.

Moreover, in the authors' opinion, the fractional description presents an additional advantage of a fundamental nature. It can be argued that the relaxation times in classical models based on several Maxwell arms are not material properties in the strictest sense of the word. Indeed, their determination depends on the temporal extent of the measured viscoelastic response. If a relaxation (or creep) curve is available over a certain number of time logarithmic decades, the decision regarding relaxation times to be employed (and whose 'weights' are then computed as a result of numerical fitting) is indeed arbitrary. Typically, relaxation times are chosen equispaced on a logarithmic scale, but there is no reason other than practicality to do so. The authors believe that fractional calculus is indeed a more fundamental description of the viscoelastic response as its physical foundation seems far more solid [42]. The material parameters of a viscoelastic model based on fractional calculus are hence believed to possibly be objective properties of the material under scrutiny.

Fractional viscoelasticity also entails a computational cost with respect to the use of exponential relaxation functions. For the latter, a closed-form second-order accurate time-integration scheme

can be used based on a well-known recursive formula, which exploits the properties of exponential functions [30]. The recursive nature of the formula means that the algorithm only requires the knowledge of history variables at the beginning of a time increment, without the need of all the previous values of strains and history variables. Furthermore, the recursive scheme can also be extended to the case of non-linear viscoelasticity [31].

Instead, time-integration algorithms for a fractional viscoelastic model require storing and using the entire strain history at each point or, in the case of a CZM, the entire relative-displacement history. In other words, for the exact time integration, it would not be possible for fractional models to make use of a finite number of history variables; this is immediate upon considering the rheological interpretation of a fractional model in terms of a 'fractal' rheological structure [32]. In practice, the numerical solution of the nonlinear structural problem can only be determined by discretising the time domain into a sequence of time increments, which entails an approximation error *per se*. For the particular algorithm considered in this work, based on the Grünwald-Letnikov expression of the fractional derivative, a further element influencing the cost and the accuracy of the analysis is the time step with which the history is sampled.

The paper is organised as follows. Firstly, the essentials of fractional viscoelasticity are reviewed in Section 2, after which the general formulation of the proposed CZM is presented in Section 3. The formulation is then closed by presenting and discussing the proposed evolution law for the damage internal variable in Section 3.1. After a summary of the input parameters of the model provided in Section 3.2, the time-integration algorithm adopted to solve the CZM is described Sections 3.3, 3.4 and 3.5. In Section 4, numerical results are presented, including a successful validation against experimental results for a DCB made of steel adherends bonded through a rubber interface. In this section, a convergence analysis is also included to show the accuracy of the time and spatial discretisations chosen, and the results of a sensitivity analysis with respect to the model input parameters are then reported, also to explain how these parameters have been calibrated. Finally, in Section 5, conclusive remarks are made, and the future outlook of this research is sketched.

2. FRACTIONAL VISCOELASTICITY

2.1. Essential concepts of fractional calculus

Fractional calculus is a branch of analysis dealing with the meaning and implications of defining differential operators of fractional order, for example $D_x^\nu = \frac{d^\nu}{dx^\nu}$ when $\nu \notin \mathcal{N}$, $\mathcal{N}$ standing for the set of natural numbers. The subject, whose historic origins are traced back to a letter to G. L' Hôpital from W. Leibniz in the year 1695 [33], has attracted some attention from the viscoelasticity community as a result of some significant advantages entailed by the use of fractional derivatives in the development of viscoelastic models. We will herein briefly present the essential concepts, referring the reader to [29, 34, 35] for further details.

The key idea is to extend Cauchy's formula for repeated integration

$$\int_0^t \int_0^{\xi_1} \dots \int_0^{\xi_{n-1}} f(\xi_n) \, d\xi_n \dots d\xi_1 = \frac{1}{(n-1)!} \int_0^t (t-\tau)^{n-1} f(\tau) d\tau, \quad n \in \mathcal{N} \tag{1}$$

from the case $n \in \mathcal{N}$ to $\nu \in \Re^{++}$ by using the Gamma function Γ, because by definition, $\Gamma(n) = (n-1)!$ for $n \in \mathcal{N}$. The Riemann–Liouville fractional integral of order $\nu > 0$ is then:

$$_0 I_t^\nu f(t) = \frac{1}{\Gamma(\nu-1)} \int_0^t (t-\tau)^{\nu-1} f(\tau) d\tau, \quad t > 0, \quad \nu \in \Re^{++} \tag{2}$$

Different fractional derivative definitions [34] can be based on the composition of the classical derivative and fractional integral operators, yielding the Riemann–Liouville fractional derivative:

$$_0 D_t^\nu f(t) = \begin{cases} \frac{1}{\Gamma(m-\nu)} \frac{d^m}{dt^m} \int_0^t \frac{f(\tau)d\tau}{(t-\tau)^{\nu+1-m}} & \text{if } m-1 < \nu < m, \, m \in \mathcal{N} \\ \frac{d^\nu}{dt^\nu} f(t) & \text{if } \nu \in \mathcal{N} \end{cases} \tag{3}$$

or the inverse composition, i.e., the composition of the fractional integral and classical derivative operators, yielding the Caputo fractional derivative:

$$
{}_0^* D_t^v f(t) = \begin{cases} \frac{1}{\Gamma(m-v)} \int_0^t \frac{f^{(m)}(\tau)\mathrm{d}\tau}{(t-\tau)^{v+1-m}} & \text{if } m - 1 < v < m, \, m \in \mathcal{N} \\ \frac{\mathrm{d}^v}{\mathrm{d}t^v} f(t) & \text{if } v \in \mathcal{N} \end{cases}
\tag{4}
$$

where $f^{(m)} = d^m f / dt^m$.

The Caputo definition has the advantage that integer-order initial conditions are needed only [34], while initial conditions of fractional type have to be considered for the Riemann–Liouville formulation, for which a physical interpretation is provided in [36] (see also [34, p.40] for compatibility conditions for stress and strain in the most general case). The problem of initial conditions in fractional differential formulations is avoided in the present work by the physically plausible assumption of nihil strain (and stress) for negative times, which is satisfied for the numerical application considered in Section 4. This is because in this case the total equivalence of the Riemann–Liouville and Caputo definitions can be proved [34, 35].

It is worth noting that in the numerical implementation of the model proposed in this paper, we use neither of the aforementioned two definitions, resorting instead to the Grünwald–Letnikov fractional derivative later discussed in Section 3.3.1. It can be shown [35] that the latter is equivalent to the Riemann–Liouville definition (3) when $f^{(k)}$ is continuous for $k = 0, 1, \ldots, m - 1$, which is the case in the numerical applications considered in this paper, in which $0 < v < 1$, whereby continuity is the only requirement. On the other hand, the aforementioned two definitions have been recalled for the benefit of the reader interested in applying our proposed approach to cases with different and more demanding initial conditions. Furthermore, the Caputo definition (4) is used in the next section.

2.2. Fractional calculus applied to viscoelasticity

The introduction of the concept of fractional differentiation arises naturally in the study of viscoelasticity, within which, attention is restricted to uniaxial stress–strain laws and a response functional of the type

$$
\sigma(t) = \int_0^t \mathcal{J}(t - \zeta) \, \dot{\varepsilon}(\zeta) \mathrm{d}\zeta
\tag{5}
$$

where σ and ε denote the stress and strain histories, and $\mathcal{J}$ denotes the relaxation function, which completely characterises the response of an arbitrary linearly viscoelastic material. Such restriction has a physical meaning, in that only linear and bounded functionals are considered (a consequence of Riesz's Theorem, [37]); history-dependent behaviour such as plasticity is hence ruled out. A discussion on the properties of functional (5) from a purely mathematical point of view can be found in [37]; from the physical point of view, additional conditions are necessary in order to achieve compliance with the second law of thermodynamics. While referring the reader to [38–42] for an overview on general thermodynamic requirements on relaxation functions, for the purposes of this work, it is sufficient to assess the thermodynamic consistency of the proposed model directly, which will be carried out in Section 3.

What is the most relevant from the engineering point of view is the physical meaning of the relaxation function. Indeed, $\mathcal{J}$ equals the stress history experienced by a material submitted to a Heaviside-type strain history. This fact provides a procedure capable of fully characterising the material via one stress-relaxation test only, whereby the material is ideally instantaneously deformed up to a prescribed strain, and its stress response monitored while the strain is kept constant.

Historically, to represent the relaxation function, linear combinations of exponential functions have been extensively used, the reason being that exponentials naturally arise as solutions of the constant-coefficients linear differential equations typical of the rheological representation of viscoelasticity. More precisely, exploiting such rheological analogy, this is equivalent to adding

Maxwell arms, each made of a dashpot and a spring in series, with different relaxation times, remembering that exponential functions form a complete basis for continuous monotonic functions. However, such a procedure adds complexity to the problem of determining the material constants, and is furthermore ill-posed in general [43], see also the discussion in [35, Section 6.4].

The aforementioned considerations suggest that linear combinations of exponentials are not the most suited functions to represent the real materials' behaviour. Instead, starting from the work of Nutting [44] in the early 1920s, it was noted that, for many polymers, stress relaxation is naturally described by power-law-type functions with exponents ν between 0 and 1. Following this observation, if a power law is used as relaxation function

$$\sigma(t) = \int_0^t A(t-s)^{-\nu} \dot{\varepsilon}(s) \mathrm{d}s \qquad 0 < \nu < 1 \tag{6}$$

upon setting $A = c/\Gamma(1-\nu)$, c being a positive scalar, the following expression is obtained

$$\sigma(t) = c \int_0^t \frac{1}{\Gamma(1-\nu)}(t-s)^{-\nu} \dot{\varepsilon}(s)\,\mathrm{d}s \tag{7}$$

The integral on the right-hand side coincides with the Caputo definition (4) of fractional derivative of ε of order ν, and because $0 < \nu < 1$ then $m = 1$. It results then:

$$\sigma(t) = c\ _0D_t{}^\nu \varepsilon \tag{8}$$

Equation (8) is the first historic archetype of fractional-derivative viscoelasticity, the Scott-Blair model from the English researcher who first introduced it [45]. This model represents a mechanical behaviour, which interpolates between a Newtonian fluid (for $\nu = 1$) and a hookean solid (for $\nu = 0$). Consequently, the rheological element characterised by a constitutive law as in Equation (8) has been named 'springpot' [46]. The springpot can be used *in lieu* of Newtonian dampers in creating rheological models together with springs. For simplicity, the differential representation of linear viscoelasticity is now employed to highlight as much as possible the physical counterpart to the mathematical operations presented.

The classical standard linear solid (SLS) (or Zener, [47]) model is governed by the following response functional

$$\sigma(t) = \int_0^t \left(E_1 + E_2\,e^{-\frac{t-\zeta}{\lambda}} \right) \dot{\varepsilon}(\zeta)\,\mathrm{d}\zeta \tag{9}$$

where λ stands for the relaxation time and, denoting by E_∞ the slow-limit (fully relaxed) elastic constant and by E_0 the fast-limit elastic constant, $E_1 = E_\infty$ and $E_2 = E_0 - E_\infty$. In Sections 3 and 4, we will also use the following notation, widely adopted in viscoelasticity:

$$E_1 = E_\infty = \mu\,E_0 \qquad E_2 = (1-\mu)\,E_0 \tag{10}$$

where μ represents the ratio between the slow-limit and fast-limit moduli.

In the rheological representation of the SLS depicted in Figure 1(a), E_1 and E_2 are the stiffnesses of the two springs in the elastic arm and in the Maxell arm, respectively, while $\lambda = \eta/E_2$, η being the viscosity constant of the Newtonian damper.

The representation provided by Equation (9) is equivalent to the following ordinary differential equation (ODE) (to which homogeneous initial boundary conditions are appended)

$$\sigma + \lambda\,\dot{\sigma} = E_1\,\varepsilon + \gamma\,\dot{\varepsilon} \tag{11}$$

where $\gamma = \lambda\,(E_1 + E_2) = \lambda\,E_0$. The fractional SLS model is obtained by altering the order of derivation, as follows

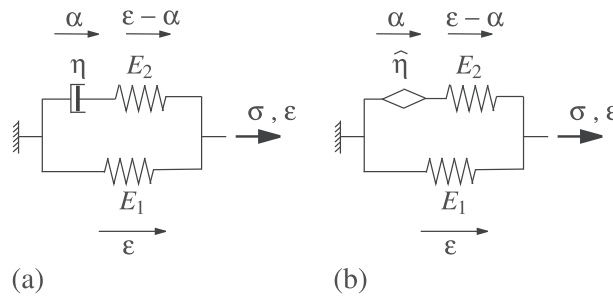$$\sigma + \hat{\lambda}\ _0D_t^\nu \sigma = E_1\,\varepsilon + \hat{\gamma}\ _0D_t^\nu \varepsilon \tag{12}$$

Figure 1. Rheological representation of the (a) classic and (b) fractional Standard Linear Solid model.

with $\nu \in (0, 1)$, whereby $\hat{\lambda} = \hat{\eta}/E_2$ and $\hat{\gamma} = \hat{\lambda}(E_1 + E_2)$ have a physical meaning similar to the classical case but are dimensionally different; see also [48]. The rheological representation of the fractional SLS model is depicted in Figure 1(b) by replacing the Newtonian damper with a springpot element with the constant $\hat{\eta}$.

Thermodynamic consistency for $0 \leqslant \nu \leqslant 1$ is proved by considering a theorem in [49] stating that if the relaxation function is monotonic decreasing, convex and tends to a non-negative asymptotic value, then the work performed on any strain path starting from equilibrium is non-negative. The same result was proved by appealing to the rheological analogy in [50]. For further details, including a more comprehensive discussion on the physical meaning of fractional viscoelasticity, we refer to [29] and references therein.

3. FORMULATION OF THE COHESIVE-ZONE MODEL

Focusing on a mode-I problem and making again the assumption that relative displacements at the interface are zero for negative times, the interface traction σ at time t at a point of an interface with memory is characterised by a (generally non-linear) functional defined on a suitable set of displacement jump histories $\delta : [0, t] \rightarrow \mathfrak{R}$.

Within the spirit of the dimensional reduction entailed by the CZM concept, whereby a thin layer is lumped on an interface whose thickness is either zero or very small, the functional dependence of the stress upon δ is assumed to be the same as that upon the strain ε in the continuum case.

The fractional SLS model is chosen as a reasonable representation of the response of the undamaged interface, and the rheological representation of its specialisation to a CZM, by replacing the strain ε with the relative displacement δ, is shown in Figure 2.

The stress response at time t of the fractional SLS model (i.e., without damage) due to a displacement jump history δ will be denoted as $\Sigma(\delta, t)$ and, for what explained earlier, is the solution of the following ODE, which is the CZM equivalent of ODE (12):

$$\sigma + \hat{\lambda} \, _0D_t^\nu \sigma = E_1 \delta + \hat{\gamma} \, _0D_t^\nu \delta \tag{13}$$

The damaging process is instead described through an internal damage variable D, whereby the overall response is given as the product of a damage term, whose evolution will be discussed in Section 3.1, and a linear functional:

$$\sigma(t) = [1 - D(t)] \Sigma(\delta, t) \tag{14}$$

It is worth remarking that σ is now a non-linear functional of δ as a result of the combination of viscoelasticity and damage.

In the analytical treatment of the cohesive-zone concept [51], the case $\delta < 0$ is not physically significant as it implies interpenetration, but, in most numerical implementations, this case has to be dealt with. The matter is addressed by assuming that, in compression, damage does not influence the response due to crack closure, rate dependence is negligible and the interface stiffness is given by a scalar K_c. Notice that, for the applications considered in this paper, the last two assumptions are physically justified by the typical behaviour of rubber under confined compression [52].
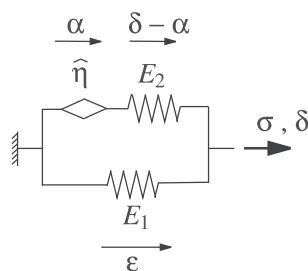
Figure 2. Rheological representation of the cohesive-zone specialisation of the fractional standard linear solid model.

3.1. Evolution law of the internal damage variable

The following evolution law for the damage variable D is assumed:

$$D = \begin{cases} 0 & \text{if } \delta_{max} \leqslant \delta_0 \\ \min\left\{1, \left(\dfrac{G_{c1}}{G_{c1} - G_{01}}\right)\left(1 - \dfrac{\delta_0}{\delta_{max}}\right)\right\} & \text{if } \delta_{max} \geqslant \delta_0 \end{cases} \tag{15}$$

where G_{c1} is the energy dissipated per unit of new crack area in the slow limit case (Figure 3(a)), δ_{max} is the maximum displacement in the previous history:

$$\delta_{max} = \delta_{max}(t) = \max_{\tau \leqslant t} \delta(\tau) \tag{16}$$

δ_0 is the value of the displacement jump at which damage starts growing in the elastic arm, and G_{01} is the elastic energy in the elastic arm when $\delta = \delta_0$, whereby it results:

$$\delta_0 = \sqrt{\frac{2\,G_{01}}{E_1}} \tag{17}$$

In the slow limit, all the stress is withstood by the elastic arm, whereby the aforementioned relationship provides the widely used bilinear law adopted for example in [53] (see Figure 3(a)).

In the general case, the energy eventually dissipated in the elastic arm of the rheological model after complete decohesion is always equal to G_{c1}. Instead, the total energy dissipated is the sum of G_{c1} and of the energies dissipated in the spring and in the springpot of the inelastic arm. This introduces rate dependence in the simulated dissipative process within the process zone at the interface.

In fact, the proposed model reproduces a bilinear traction-separation law only in the limit cases of infinitely slow or fast loading, in total analogy with how linear viscoelastic behaviour reduces to linear elastic behaviour in the fast and slow limit. This aspect could be investigated with a comprehensive treatment of the thermodynamics of the model, which is outside the scope of the present work and is instead left for the future developments of this research; this is also because it is known that, in linear viscoelasticity, the definition of the free energy is not unique. Nevertheless, to gain further insight into the rate dependence of the response predicted by our proposed model, let us limit the analysis to the case $\delta(t) \geqslant 0$ for any $t \in \Re$ and define the 'rupture' dissipation Π_r as the power dissipated within the elastic springs of the rheological representation of the model in Figure 2, i.e., the energy lost per unit of time within the springs due to the rupture of elastic bonds, which is given by:

$$\Pi_r = Y\,\dot{D} = \left[\frac{1}{2}E_1\,\delta^2(t) + \frac{1}{2}E_2\,(\delta(t) - \alpha(t))^2\right]\dot{D} \tag{18}$$

where

$$Y = \frac{1}{2}E_1\,\delta^2(t) + \frac{1}{2}E_2\,(\delta(t) - \alpha(t))^2 \tag{19}$$

physically represents the elastic energy in the two springs of the model if there was no damage in the material.

Slow limit

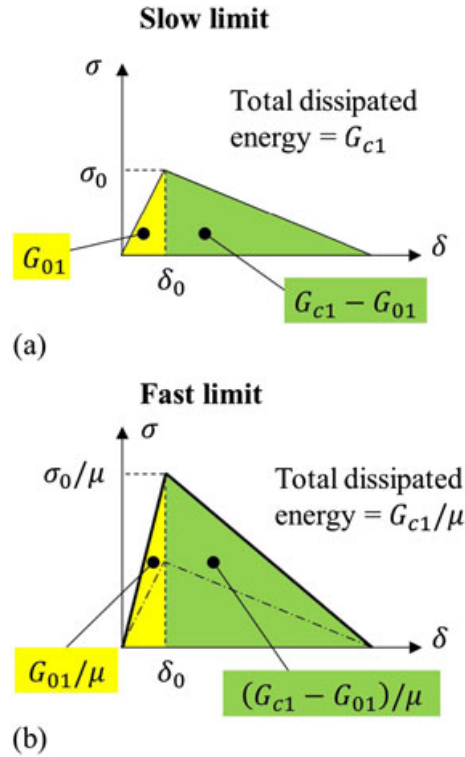
(a)

Fast limit

(b)

Figure 3. Interface stress versus relative displacement curves in the (a) slow and (b) fast limit.

In the slow limit, the fractional Maxwell arm is completely relaxed and $\alpha \to \delta$, whereby it results:

$$Y = \frac{1}{2} E_1 \delta^2 = \frac{1}{2} E_\infty \delta^2 \tag{20}$$

It is easy to verify from Equation (15) that, at any time in which $\dot{D} > 0$, it results $\delta_{max} = \delta$. Hence, when $\dot{D} > 0$, it results:

$$\delta_{max} = \delta = \sqrt{\frac{2Y}{E_1}} \tag{21}$$

Replacing (17) and (21) in Equation (15), we obtain:

$$\dot{D} > 0 \Leftrightarrow D = \left(\frac{G_{c1}}{G_{c1} - G_{01}} \right) \left(1 - \sqrt{\frac{G_{01}}{Y}} \right) = \frac{1}{\beta} \left(1 - \sqrt{\frac{G_{01}}{Y}} \right) \tag{22}$$

where β is given by:

$$\beta = 1 - \frac{G_{01}}{G_{c1}} \tag{23}$$

Inverting Equation (22), we obtain the following damage growth criterion:

$$\dot{D} > 0 \Leftrightarrow Y = \frac{G_{01}}{(1 - \beta D)^2} \tag{24}$$

and, integrating the rupture dissipation, the 'rupture' energy G_{cr} is obtained:

$$G_{cr} = \int_0^{+\infty} \Pi_r \, dt = \int_0^{+\infty} Y \dot{D} \, dt = \int_0^1 \frac{G_{01}}{(1 - \beta D)^2} \, dD = \frac{G_{01}}{(1 - \beta)} = G_{c1} \tag{25}$$

Because, in the slow limit, the dissipation within the springpot tends to zero, the (total) fracture energy denoted in the sequel as G_{ct} is equal to the rupture energy and reduces to the lower limit G_{c1}.

In the fast limit, $\alpha \to 0$, whereby it results:

$$Y = \frac{1}{2}(E_1 + E_2)\,\delta^2 = \frac{1}{2}E_0\,\delta^2 = \frac{1}{\mu}\left(\frac{1}{2}E_1\,\delta^2\right) \tag{26}$$

Following the same developments as in the slow-limit case, it is easy to verify that in the fast-limit case, the damage growth criterion becomes:

$$\dot{D} > 0 \Leftrightarrow Y = \frac{G_{01}}{\mu\,(1 - \beta\,D)^2} \tag{27}$$

and the rupture energy is given by:

$$G_{cr} = \int_0^{+\infty} Y\,\dot{D}\,dt = \int_0^1 \frac{G_{01}}{\mu\,(1 - \beta\,D)^2}\,dD = \frac{G_{01}}{\mu\,(1 - \beta)} = \frac{G_{c1}}{\mu} \tag{28}$$

As for the slow-limit case, the dissipation in the springpot tends to zero in the fast-limit case, too, whereby the (total) fracture energy G_{ct} is again equal to the rupture energy G_{cr} and reaches the upper limit G_{c1}/μ.

Effectively, the aforementioned equations show that, in the fast limit, a bilinear curve is again followed and, as shown in Figure 3(b), the relative displacement corresponding to the onset of softening does not change and is again equal to δ_0, whereas the slope of the initial elastic part is amplified by a factor $1/\mu$. Hence, the peak stress σ_0 and the total energy dissipated per unit of surface are amplified by the same factor too.

The main principle behind the proposed damage evolution law is that damage is driven only by the elastic energy in that, regardless of the relative-displacement speed, when the elastic energy reaches a (rate-independent) threshold in each of the 'elastic elements' of the system, damage increases. A rigorous application of this principle in an engineering context would require a unique definition of free energy, which is lacking [54] (and would also entail consideration that at finite speeds some elastic energy is stored within the springpot, see [55]). While this will be pursued in future developments, in this work, we use the evolution law given by Equation (15) as it satisfies the following main requirements: (i) damage evolution is a rate-independent function of the opening displacement; (ii) in the slow limit the total energy dissipated (per unit of surface) is equal to G_{c1}; (iii) in the fast limit the total energy dissipated is equal to G_{c1}/μ; and (iv) a smooth transition between the two responses in the slow and the fast limit occurs.

Remark 3.1

Even if the model has not been developed following an energetic approach, it is possible to demonstrate its thermodynamic consistency. To this end, let us observe that the traction-separation law could be interpreted as originating from a fractional rheological model in series with a 'damage' element, whose only contribution is to scale the stress in the fractional element by a factor given by the damage state. The thermodynamic consistency of the fractional rheological model alone, i.e., in absence of damage, is guaranteed by the fact that the relaxation function for the model satisfies the hypotheses of the theorem in [49] which was already discussed at the end of Section 2.2. Furthermore, according with the evolution law (15), along an arbitrary process, either damage increases or stays constant. In the latter, thermodynamic consistency is given by the fact the fractional element is consistent itself. In the former, the total dissipation will be greater than the dissipation in the fractional element, which is already non-negative. Hence, the total dissipation is always non-negative. ∎

3.2. Model parameters

The following seven parameters are chosen as direct input material constants for the model: G_{c1}, σ_0, β, $\hat{\lambda}$, μ, K_c and ν. From these, all the other parameters can be determined. The critical relative displacement δ_c at which cohesion is lost (see Figure 3) is given by:

$$\delta_c = \frac{2\,G_{c1}}{\sigma_0} \tag{29}$$

Parameter β can be seen as a sort of ductility of the model and allows to find δ_0 and G_{01} from δ_c and G_{c1}:

$$\delta_0 = (1 - \beta)\,\delta_c \qquad G_{01} = (1 - \beta)\,G_{c1} \tag{30}$$

The stiffness values of the two springs, E_1 and E_2, are then given by:

$$E_1 = \frac{\sigma_0}{\delta_0} \qquad E_2 = \frac{(1 - \mu)}{\mu}\,E_1 \tag{31}$$

3.3. Algorithmic solution via the Grünwald-Letnikov fractional derivative

Numerical computations in the case of fractional models are more complicated than in the case of an exponential relaxation function, for which a recursive algorithm can be formulated [30], or in general viscoelastic material models formulated within the framework of thermodynamics with internal variables [56], for which incremental variational schemes are available [57, 58]. Such schemes do not apply in general to fractional viscoelastic formulations.

Numerical fractional differentiation/integration algorithms can be classified into three categories [59]. The first category comprises algorithms whose starting point is the Riemann–Liouville definition; in Equation (2) the integral expression can be numerically evaluated using various techniques from numerical integration. The second category relies instead on an alternative definition of fractional derivative/integral [60], which was later shown to be equivalent to the Riemann–Liouville definition [61] for sufficiently smooth functions. The third type of approach is based on exploiting the linearity of the viscoelastic functionals by approximating the strain history as a piecewise constant function and superimposing the responses due to each increment; this is the approach historically used by Boltzmann [62].

In this work, we followed the second of these strategies, based on the the Grünwald-Letnikov definition of fractional derivative. Such a numerical approximation strategy has been used in [63, 64], among others.

3.3.1. Grünwald-Letnikov fractional derivative.

The Grünwald-Letnikov expression of the fractional derivative is derived from the observation that the usual, first integer-order derivative can be approximated *via* a backward difference scheme

$$\frac{\mathrm{d}f(t)}{\mathrm{d}t} = \lim_{\Delta t \to 0} \frac{1}{\Delta t}[f(t) - f(t - \Delta t)] \tag{32}$$

so that iterated applications yield

$$\frac{\mathrm{d}^2 f(t)}{\mathrm{d}t^2} = \lim_{\Delta t \to 0} \frac{1}{\Delta t^2}[f(t) - 2f(t - \Delta t) + f(t - 2\Delta t)] \tag{33}$$

$$\frac{\mathrm{d}^3 f(t)}{\mathrm{d}t^3} = \lim_{\Delta t \to 0} \frac{1}{\Delta t^3}[f(t) - 3f(t - \Delta t) + 3f(t - 2\Delta t) - f(t - 3\Delta t)] \tag{34}$$

which can be generalised using induction to

$$\frac{\mathrm{d}^n f(t)}{\mathrm{d}t^n} = \lim_{\Delta t \to 0}\left[\frac{1}{\Delta t^n}\sum_{j=0}^{n}(-1)^j\binom{n}{j}f(t - j\Delta t)\right] \tag{35}$$

Following [63], after setting $\Delta t = t/N$, Equation (35) can be written

$$\frac{\mathrm{d}^n f(t)}{\mathrm{d}t^n} = \lim_{N \to \infty}\left[\left(\frac{t}{N}\right)^{-n}\sum_{j=0}^{N-1}(-1)^j\binom{n}{j}f\left(t - j\frac{t}{N}\right)\right] \tag{36}$$

In order to allow the applicability of Equation (36) outside integer-order derivation, the binomial coefficient definition is extended, for $v \in \Re$ and $j \in \mathcal{N}$ as

$$\binom{v}{j} = \begin{cases} \frac{v(v-1)(v-2)\ldots(v-j+1)}{j!} & \text{for} \quad j > 0 \\ 1 & \text{for} \quad j = 0 \end{cases} \tag{37}$$

Then $(-1)^j \binom{v}{j}$ can be expressed as

$$(-1)^j \binom{v}{j} = (-1)^j \frac{v(v-1)(v-2)\ldots(v-j+2)(v-j+1)}{j!} \tag{38}$$

which leads to

$$(-1)^j \binom{v}{j} = \binom{j-v-1}{j} = \frac{\Gamma(j-v)}{\Gamma(-v)\Gamma(j+1)} \tag{39}$$

where Γ stands for the Γ function. Replacing expression (39) in Equation (36) provides the following formula, in which v is required only to belong to $\Re$

$$\frac{d^v f(t)}{dt^v} = \lim_{N \to \infty} \left[\left(\frac{t}{N}\right)^{-v} \sum_{j=0}^{N-1} \frac{\Gamma(j-v)}{\Gamma(-v)\Gamma(j+1)} f\left(t - j\frac{t}{N}\right) \right] \tag{40}$$

It can be recognised how the given definition agrees with the usual integer-order derivation definition for $v = n > 0, n \in \mathcal{N}$, in that in this case, only the first $n + 1$ of the so-called Grünwald-Letnikov coefficients A_j

$$A_{j+1} = \frac{\Gamma(j-v)}{\Gamma(-v)\Gamma(j+1)} \tag{41}$$

are nonzero due to properties of the Γ function. If $v \notin \mathcal{N}$, then all the A_j are different from zero, which underlines how in general the fractional derivative is a non-local operator.

The Grünwald-Letnikov coefficients obey the useful recursive formula [63]:

$$A_{j+1} = \frac{\Gamma(j-v)}{\Gamma(-v)\Gamma(j+1)} = \frac{j-1-v}{j} \frac{\Gamma(j-1-v)}{\Gamma(-v)\Gamma(j)} = \frac{j-1-v}{j} A_j, A_1 = 1 \tag{42}$$

which is very useful in that definition (41) could lead to numerical problems if v is close to an integer or for large iteration index.

3.3.2. Numerical approximation of the Grünwald-Letnikov derivative. In general, the Grünwald-Letnikov definition requires handling an infinite series expansion, the time step t/N tending to zero. To overcome this impracticality, it is natural to consider a finite sum instead of the infinite sum in Equation (40), leading to the following approximation:

$$\frac{d^v f(t)}{dt^v} = \lim_{N \to \infty} \left[\left(\frac{t}{N}\right)^{-v} \sum_{j=0}^{N-1} A_{j+1} f\left(t - j\frac{t}{N}\right) \right] \cong$$
$$\cong \left(\frac{t}{N_t}\right)^{-v} \sum_{j=0}^{N_t-1} A_{j+1} f\left(t - j\frac{t}{N_t}\right) \tag{43}$$

The value of N_t fixes the time step used for sampling the function in the Grünwald-Letnikov and is to be chosen as a compromise between accuracy and computational time.

Remark 3.2
The efficiency in the computation of the Grünwald–Letnikov derivative at fixed N_t can further be improved by remembering the Grünwald–Letnikov coefficients are in absolute value decreasing for fractional coefficients $0 < \nu < 1$, a manifestation of the fading-memory principle. This suggests that an initial part of the history could be ignored in the summation leading to a relatively small error whose value can be controlled. Other ways to reduce the computational cost include a small modification of the aforementioned derivation leading to the use of different time steps for different parts of the history, smaller for the 'more recent' part of the history and larger for the initial part of it [63]. However, these methods are not considered in this paper also because the numerical applications are not computationally demanding, whereas the focus is on the derivation and validation of the model. On the other hand, the computational cost entailed by the use of fractional calculus is a key limitation whereby it will be essential in the future to enhance the implementation of the proposed model with methods to improve its computational efficiency.

It is convenient to set

$$\Delta t_{GL} = \frac{t}{N_t} \tag{44}$$

where Δt_{GL} denotes the sampling time increment, i.e., the backward time increment with which the history is sampled to compute the approximation of the Grünwald–Letnikov derivative, which is generally not equal to the time increment used in an incremental non-linear solution strategy.

If one keeps N_t fixed, then Δt_{GL} gradually increases during the analysis, i.e., with increasing t, which may lead to a progressive decrease of accuracy in the computation of the derivative.

It is therefore more convenient to fix Δt_{GL} so that, considering zero values for negative times, the actual number of sampling points N_h is given at each time t by:

$$N_h = \text{Int}\left(\frac{t}{\Delta t_{GL}}\right) + 1 \tag{45}$$

where $\text{Int}(x)$ denotes the integer part of $x \in \Re$.

Summarising, the approximated expression of the Grünwald–Letnikov fractional derivative is obtained by replacing relationships (44) into Equation (43):

$$\frac{\mathrm{d}^\nu f(t)}{\mathrm{d}t^\nu} \cong \Delta t_{GL}^{-\nu} \sum_{j=0}^{N_h-1} A_{j+1} f\left(t - j\Delta t_{GL}\right) \tag{46}$$

where N_h is given by Equation (45), while Δt_{GL} is an algorithmic parameter to be suitably calibrated aiming at a convenient compromise between accuracy and computational cost.

3.4. Numerical solution of the fractional standard linear solid cohesive model

By using Equation (46) to obtain a numerical approximation of the two fractional derivatives of σ and δ and observing that $A_1 = 1$, one has:

$$_0 D_t^\nu \sigma \cong \Delta t_{GL}^{-\nu} \left[\sigma(t) + S_\sigma\right] \qquad _0 D_t^\nu \delta \cong \Delta t_{GL}^{-\nu} \left[\delta(t) + S_\delta\right] \tag{47}$$

where:

$$S_\sigma = \sum_{j=1}^{N_h-1} A_{j+1} \sigma\left(t - j\Delta t_{GL}\right) \qquad S_\delta = \sum_{j=1}^{N_h-1} A_{j+1} \delta\left(t - j\Delta t_{GL}\right) \tag{48}$$

Replacing the aforementioned expressions into Equation (13), and making the dependence on t explicit, we obtain:

$$\sigma(t) + \hat{\lambda}\,\Delta t_{GL}^{-\nu}\left[\sigma(t) + S_\sigma\right] = E_1\,\delta(t) + \hat{\gamma}\,\Delta t_{GL}^{-\nu}\left[\delta(t) + S_\delta\right] \tag{49}$$

Solving for $\sigma(t)$ provides the following numerical (approximate) solution of the response Σ of the cohesive SLS model, i.e., in absence of damage:

$$\Sigma(\delta, t) = \left(1 + \hat{\lambda}\,\Delta t_{GL}^{-\nu}\right)^{-1}\left[\left(E_1 + \hat{\gamma}\,\Delta t_{GL}^{-\nu}\right)\delta(t) + \Delta t_{GL}^{-\nu}\left(\hat{\gamma}\,S_\delta - \hat{\lambda}\,S_\sigma\right)\right] \tag{50}$$

3.5. Finite-step solution of the cohesive-zone model

Having determined the damage evolution law in Section 3.1 and the numerical approximation for the solution of the fractional SLS cohesive model in Section 3.4, in this section, we can combine these together using Equation (14) to derive the time-integration algorithm to determine the response of the CZM.

Recalling that, we assume the displacement-jump history to be nihil before $t = 0$ the time interval over which the computation is to be carried out, $[0, T]$, is discretised into a partition of N_{inc} time increments:

$$[0, T] = \bigcup_{n=1}^{N_{inc}} [t_n, t_{n+1}] \qquad\qquad t_{n+1} = t_n + \Delta t_n \tag{51}$$

In the n-th time increment, the times at the start and the end of the increment are t_n and t_{n+1}, respectively. Setting $\sigma_{n+1} = \sigma(t_{n+1})$, $\delta_{n+1} = \delta(t_{n+1})$, $D_{n+1} = D(t_{n+1})$ and $\Sigma_{n+1} = \Sigma(\delta_{n+1}, t_{n+1})$, in the framework of a non-linear displacement-based (finite-element for example, but not necessarily) solution scheme, the problem is relative-displacement driven, whereby δ_{n+1} is assigned while σ_{n+1} and D_{n+1} are computed as follows:

$$\sigma_{n+1} = \begin{cases} (1 - D_{n+1})\,\Sigma_{n+1} & \text{if } \delta_{n+1} \geqslant 0 \\ K_c\,\delta_{n+1} & \text{if } \delta_{n+1} < 0 \end{cases} \tag{52}$$

where from Equation (50):

$$\begin{aligned}\Sigma_{n+1} = \left(1 + \hat{\lambda}\,\Delta t_{GL}^{-\nu}\right)^{-1}\Big[&\left(E_1 + \hat{\gamma}\,\Delta t_{GL}^{-\nu}\right)\delta(t) + \\ &+ \Delta t_{GL}^{-\nu}\left(\hat{\gamma}\,S_{\delta,n+1} - \hat{\lambda}\,S_{\sigma,n+1}\right)\Big]\end{aligned} \tag{53}$$

in which $S_{\delta,n+1}$ and $S_{\sigma,n+1}$ are given by:

$$S_{\sigma,n+1} = \sum_{j=1}^{N_h-1} A_{j+1}\,\sigma\left(t_{n+1} - j\,\Delta t_{GL}\right) \qquad S_{\delta,n+1} = \sum_{j=1}^{N_h-1} A_{j+1}\,\delta\left(t_{n+1} - j\,\Delta t_{GL}\right) \tag{54}$$

Instead, making also use of (23), D_{n+1} in Equation (53) is given by:

$$D_{n+1} = \begin{cases} 0 & \text{if } \delta_{max,n+1} \leqslant \delta_0 \\ \min\left\{1, \frac{1}{\beta}\left(1 - \frac{\delta_0}{\delta_{max,n+1}}\right)\right\} & \text{if } \delta_{max,n+1} \geqslant \delta_0 \end{cases} \tag{55}$$

where the current maximum displacement $\delta_{max,n+1}$ is a history variable in the model, which is initialised as $\delta_{max,0} = 0$ at the beginning of the first increment and is updated at each increment as follows:

$$\delta_{max,n+1} = \max\{\delta_{n+1}, \delta_{max,n}\} \tag{56}$$

Remark 3.3

It is worth noting that, in general, the time increment Δt_n used in the Newton–Raphson scheme is chosen using an automatic incrementation procedure, whereby Δt_n increases or decreases according to the rate of convergence in each increment, within user defined maximum and minimum values. Instead, the time increment Δt_{GL} defining the sampling points of the Grünwald–Letnikov summation is fixed, whereby the sampling points do not generally coincide with the time increments of the

analysis. This issue is circumvented by linearly interpolating the relative-displacement and stress history between the Newton–Raphson time steps.

Following [63], we take Δt_{GL} equal to the maximum value for the time increment Δt_n set by the user in the Newton-Raphson solution scheme, whereby it always results $\Delta t_{GL} \geqslant \Delta t_n$. This means that we only need values of the stress history already computed and, instead, do not need to take any extrapolation beyond the value of the stress computed at the last converged increment.

3.5.1. Tangent interface stiffness. As the Newton–Raphson method is used for the solution of the structural problem, to preserve quadratic convergence the (algorithmic) tangent interface stiffness is needed, which is easily obtained as follows:

$$\frac{d\sigma_{n+1}}{d\delta_{n+1}} = \begin{cases} (1 - D_{n+1})\,K_t - \frac{dD_{n+1}}{d\delta_{n+1}}\,\Sigma_{n+1} & \text{if } \delta_{n+1} \geqslant 0 \\ K_c & \text{if } \delta_{n+1} < 0 \end{cases} \tag{57}$$

where:

$$K_t = \left(1 + \hat{\lambda}\,\Delta t_{GL}^{-\nu}\right)^{-1} \left(E_1 + \hat{\gamma}\,\Delta t_{GL}^{-\nu}\right) \tag{58}$$

and

$$\frac{dD_{n+1}}{d\delta_{n+1}} = \begin{cases} 0 & \begin{aligned}&\text{if } \delta_{max,n+1} \leqslant \delta_0 \\ &\text{or } \delta_{max,n+1} \geqslant \delta_c \\ &\text{or } \delta_{n+1} < \delta_{max,n+1}\end{aligned} \\ \left(\frac{G_c}{G_c - G_0}\right)\frac{\delta_0}{\delta_{n+1}^2} & \text{if } \delta_0 < \delta_{n+1} = \delta_{max,n+1} < \delta_c \end{cases} \tag{59}$$

4. NUMERICAL RESULTS AND EXPERIMENTAL VALIDATION

The fractional-calculus-based CZM presented in Section 3 has been implemented into a user subroutine for the finite-element code ABAQUS, version 6.12.2 (Dassault Systemes, Velizy-Villacoublay Cedex, France), as constitutive law of interface elements.

4.1. Interface stress versus relative displacement for different speeds

To appreciate the response provided by the proposed CZM, the response of a single interface point is studied in this section. To this end, a total relative displacement of 5 mm has been prescribed with increments of 0.1 mm and at constant speed. The interface stress was computed at each increment and the numerical test was repeated for different prescribed speeds.

The model input parameters used are reported in Table I and are the same as those used in the numerical application reported in Section 4.3. Table II also reports some other parameters which can be derived from the input material constants of Table I, as they are useful to interpret the numerical results.

Figure 4 reports the interface stress against the prescribed relative displacement for the different applied speeds and shows that within a range of about 20 logarithmic decades of prescribed speeds, the interface response varies between the slow-limit and the fast-limit bilinear responses, exactly as

Table I. Input parameters used for the rubber interface.

G_{c1} (N mm^{-1})	σ_0 (MPa)	β	$\hat{\lambda}$ (s$^\nu$)	μ	ν	K_c (N mm^{-3})
1.50	0.75	0.6	2.3	0.049	0.3	490

Table II. Indirect parameters dependent on input parameters.

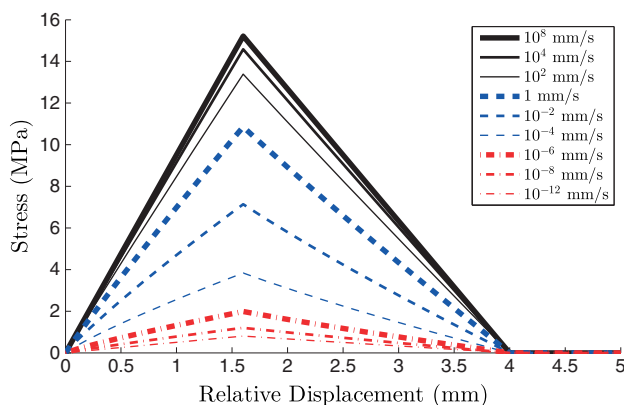| δ_0 (mm)	δ_c (mm)	E_1 (N mm^{-3})	E_2 (N mm^{-3})	G_{c1}/μ (N mm^{-1})	σ_0/μ (MPa)
1.6	4.0	0.469	9.8	30.61	15.31

Figure 4. Interface stress versus prescribed displacements for different prescribed relative displacement speeds.
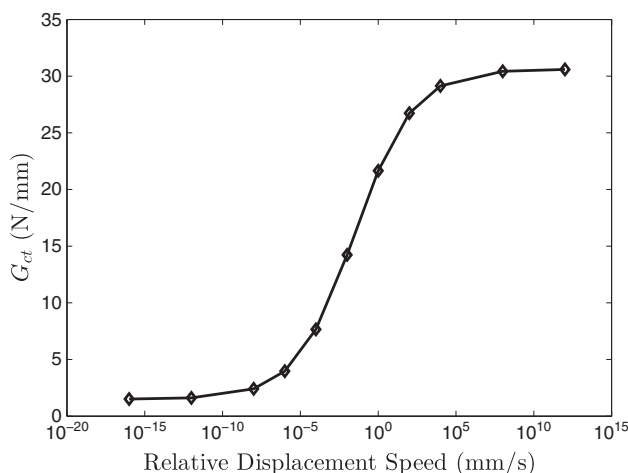

Figure 5. Total dissipated energy per unit of surface G_{ct} versus prescribed relative-displacement speed.

shown in Figure 3. The peak stress also varies from the slow limit σ_0 to the fast limit σ_0/μ, while the initial slope varies from the slow limit value $E_1 = E_\infty$ to the fast limit value $E_0 = E_1 + E_2$.

Figure 5 reports the total energy dissipated per unit of surface, G_{ct}, against the prescribed speed. As expected, the curve has a sigmoidal shape tending for infinitely low speeds to the slow limit G_{c1} and for infinitely high speed to the fast limit G_{c1}/μ. It is interesting to notice that in a range of approximately 5 logarithmic decades, between the speeds of 10^{-4} and 10^1 mm/s, the curve is very close to be linear. This observation will turn out to be useful to better interpret the results of Section 4.3.

4.2. Experimental testing

A 25mm wide DCB specimen made of 8 mm thick steel arms separated by a 1 mm thick interface of styrene butadiene rubber/natural rubber (SBR/NR) blend rubber has been tested under displacement control at six different rates of the monotonically increasing prescribed cross-head displacement, equal to 0.01, 0.1, 1, 10, 100 and 500 mm/min^{-1}. For each speed, two specimens were tested, except for the speed of 10 mm/min, for which four specimens were tested to reduce the scatter between the initial two tests, which for the other test speeds was considered acceptably narrow. The adherends were washed in an aqueous solution, then grit-blasted, then treated with a commercially available rubber–metal bonding system under controlled temperature and humidity. Hot-moulding at 145 ^{o}C for 80 min followed. The geometry of the specimen is sketched in Figure 6. A summary of all

test results is presented in Figure 7 and a close-up of the cohesive zone during one of the tests is presented in Figure 8.

The DCB specimen has been chosen as the most suitable test geometry because it offers a unique advantage when compared to other possible mode-I specimen geometries such as the peel test. Indeed, sandwiching the interface of interest between two metallic arms guarantees that no rate-dependent losses other than the ones occurring within the interface are accounted for; the modelling of the T-peel test geometry on the other hand would be dependent upon a satisfactory description of the rate-dependent behaviour of the arms. As a result, the material model can be validated more efficiently.

4.3. Finite-element modelling

Due to symmetry with respect to the crack plane, only the top half of the specimen was modelled with a two-dimensional (2D) finite-element model in plane strain. The metallic arm was meshed using a uniform structured mesh of 4x100 four-node (linear) plane-strain fully integrated elements with incompatible modes. The rubber interface was modelled using 60 four-node (linear) interface elements with two integration points and a Newton–Cotes integration rule. Of course, the 2D approximation cannot capture the fact that the crack front is not a straight line, but it was shown in [65] that in general, this leads to reasonably accurate results for wide enough specimens, such as the one tested in our case.
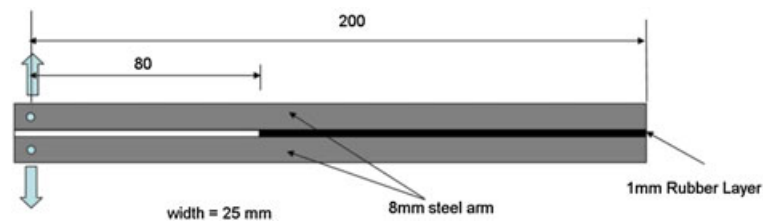
Figure 6. Geometry and loading of the tested double-cantilever-beam specimen.
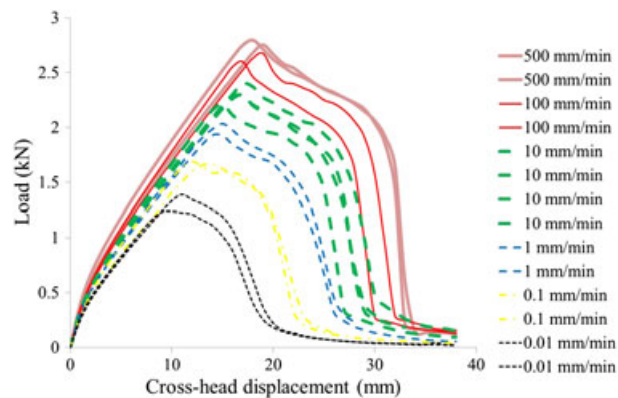
Figure 7. Summary of test results.

Figure 8. Decohesion zone during a typical test.

For the steel arms, a linear elastic model was used with a Young's modulus of 200 GPa and a Poisson's ratio of 0.3. For the rubber interface, the model parameters are those in Table I, but, because only half of the specimen has been modelled exploiting symmetry, the actual values inserted for G_{c1} for K_c were 0.75 N/mm and 980 N/mm^3, respectively.

Geometrical linearity was assumed and the boundary conditions used are reported in Figure 9, where the contour plots of the vertical direct stress component and of the interface (normal) stress are shown for an applied speed of 10 mm/min at different times of the analysis corresponding to the points marked in the load-displacement curve reported in Figure 10.

At point A, the process zone has only partially developed on the left-hand side beyond the peak of the interface tensile stress. At point B, the process zone has fully developed as the interface stress at the initial crack tip has just reduced to zero, whereby the crack starts propagating from the initial crack tip. Between points B and C, crack propagation appears to be almost self similar in nature. At point C, the zone characterised by significant compressive interface stress is approaching the end of the specimen, whereby from this point onwards, approximate self-similarity of crack propagation is gradually disrupted, although this becomes pretty clear only close to point D. Between points D and E, the distance between the two resultants of the compressive and tensile interface stresses reduces significantly, because the compressive zone cannot propagate beyond the end of the specimen. This results in significant and rapid reduction of the resultant moment and, therefore, also of the applied load, as can be seen by the nearly vertical slope of the load-deflection curve.
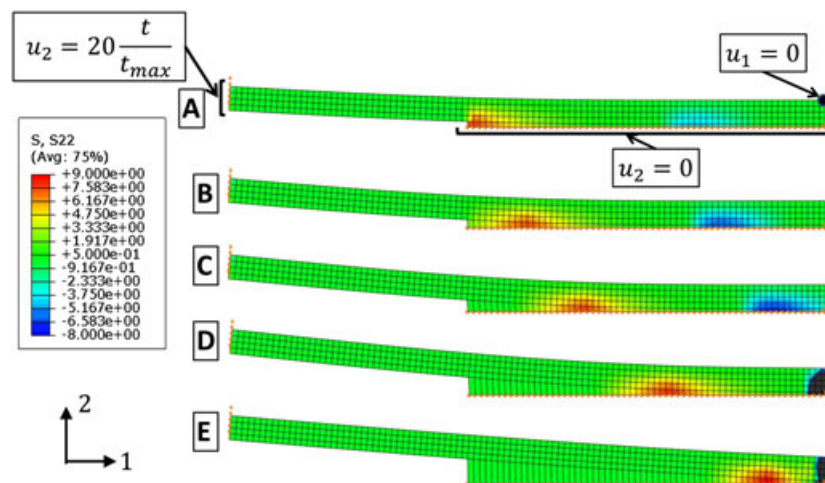

Figure 9. Contour plots of the stress component σ_{22} at different increments of the analysis conducted for the test speed of 10 mm/min, corresponding to points A, B, C, D and E of Figure 10. No amplification factor was applied to the deformed shape.
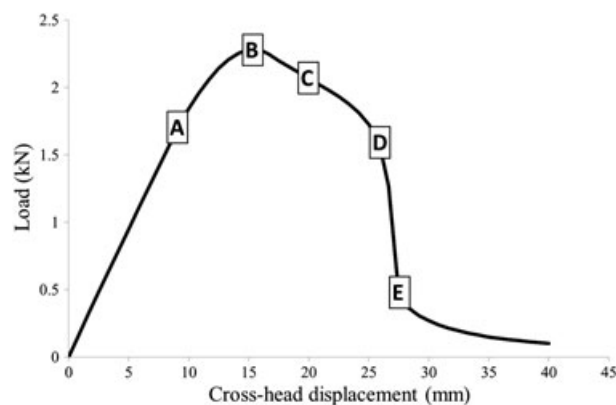

Figure 10. Load-displacement curve for the applied speed of 10 mm/min.

Figure 11 reports the experimentally measured and the numerically obtained load-displacement curves at the different prescribed speeds considered, while Figure 12 shows a comparison between the load maxima. Both of them show an excellent correlation between numerical and experimental results, which shows that the proposed CZM, with a single set of seven parameters only, is able to capture with remarkable accuracy the deformation, damage and failure of the interface within a range of speeds of almost 5 logarithmic decades.

It is worth underlying that all of the model parameters have a quite clear physical meaning, which suggests their value, or at least the value of some of them, could be identified through direct experiments on the rubber. As discussed in Section 1, this is still a challenging aspect because of the very complex mechanisms involved in the deformation, damage and failure of the rubber interface. While this will be the subject of future developments of this research, for this study, the identification of the model parameters was obtained through an empirical iterative calibration.

For each iteration of the calibration procedure, in which a new tentative set of parameters was chosen based on the results obtained with the previous ones, the results of the sensitivity analysis discussed later in Section 4.5 were of great assistance. For example, the numerically obtained curve of load maxima reported in Figure 12 is very sensitive to $\hat{\lambda}$, to the fractional exponent ν as well as to G_{c1} and μ, as discussed later in more detail. Once the load maxima were reasonably captured, iterative changes of the slow-limit strength σ_0 and the ductility parameter β were made to better fit the shape of the curves. The whole process was iterated until the correlation shown in Figures 11 and 12 was obtained. For future, more demanding, applications, systematic approaches for material parameter identification such as those considered in [66, 67] could be taken into account.

Some deviation between the experimental and numerical curves can be appreciated in the increasing part of the curves, particularly for the high speeds, where the numerically obtained stiffness
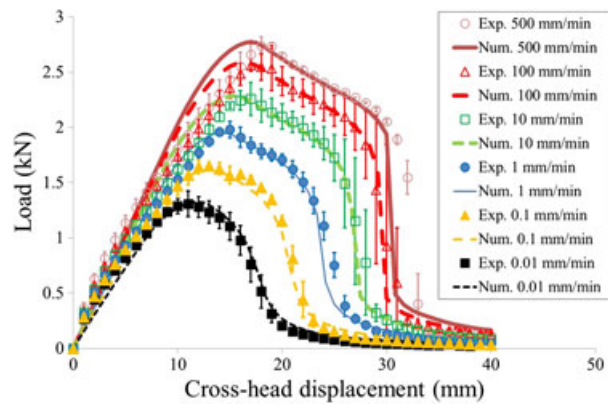

Figure 11. Experimental versus numerical load-deflection curves at different applied speeds.
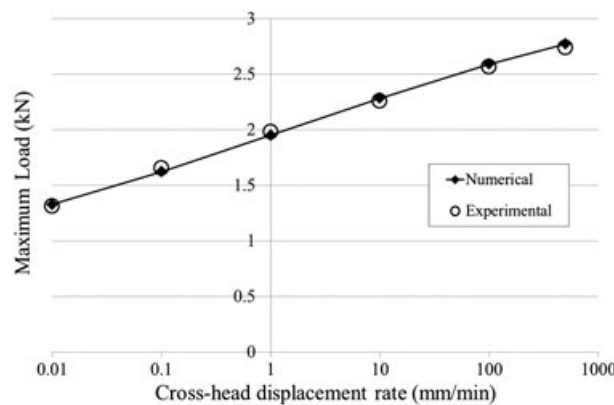

Figure 12. Experimental versus numerical load maxima at different applied speeds.

overestimates the experimental one and, to a lesser extent, for the nearly vertical descending part of the curves for the high speeds. For the latter, some discrepancy can be clearly appreciated only for the applied speed of 500 mm/min, for which the discrepancy in the increasing part is the highest too. Instead, apart from a very small deviation for the applied speed of 100 mm/min, the descending parts of the other curves were very well predicted. In the authors' opinion, while it cannot be excluded that the calibration procedure could have been pushed further to reduce these remaining small discrepancies, this was not performed because it is more likely that this shortcoming is caused by the lack of accuracy incurred by describing the rubber compound as a linear material as far as the elastic response is concerned.

This simplifying assumption was made to keep the development of the undamaged model within the established framework of linear viscoelasticity, so that the nonlinearity introduced in the model by the introduction of damage and failure is of purely material nature.

The extension of the proposed model to account for large strains of the interface will be the subject of the future developments of this research, but it is here worth remarking that the simplified assumption of linear viscoelastic undamaged behaviour is valid for many other less tough polymers. Furthermore, even for the rubber interface studied in this paper, the overall correlation between numerical and experimental results is extremely good even with this simplified hypothesis, suggesting that the dissipated energy within the process zone is far more important than the detailed shape of the traction-separation law.
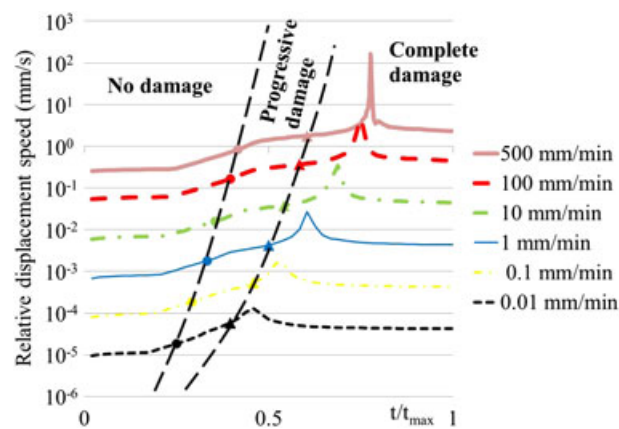

Figure 13. Relative displacement speeds on the interface at a point 20 mm from the initial crack tip versus normalised time for different applied cross-head displacement rates.
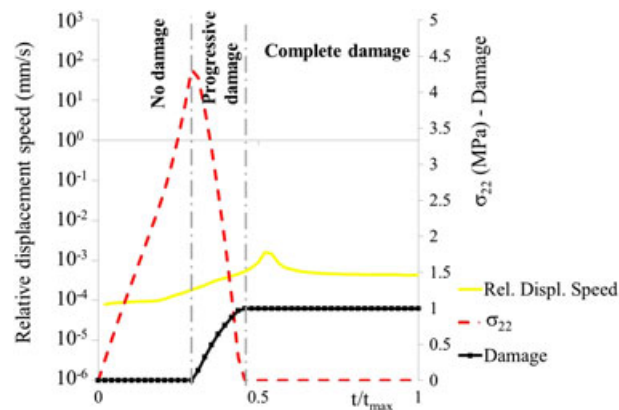

Figure 14. Relative-displacement speed, interface stress and damage at a point 20 mm from the initial crack tip versus normalised time for an applied displacement rate of 0.1 mm/min.

The almost linear semi-logarithmic relationship in Figure 12 suggests that, during the experiments, the point-wise response at each point of the interface is far enough from both the fast and the slow limit, so that they fall within the almost linear semi-logarithmic region of the curve of Figure 5.

This is confirmed by the curves shown in Figure 13, which report the relative-displacement speeds numerically computed at a point of the interface 20 mm on the right-hand side of the initial crack tip, plotted against the normalised time.

The two dashed lines in Figure 13 separate the three regions of the graph corresponding to times where no damage, progressive damage and complete damage occurs on the considered point of the interface. This is further clarified by Figure 14, where for the applied speed of 0.1 mm/min the relative-displacement speed is plotted against the normalised time together with the interface stress and the damage variable.

It can be then noticed that the sharp increase in relative displacement speed observable in each curve, which is more prominent at higher applied speeds, corresponds to times where the interface is already fully damaged. In fact, these peaks in the curve are due to the rapid increase in the speed of deformation corresponding to the nearly vertical descending slopes of the load-displacement curves of Figure 11.

Figure 13 confirms that while the interface is damaging, the relative-displacement speed for all cases falls within the region corresponding to the nearly linear part of the curve in Figure 5, more precisely between the minimum value of $1.84 \cdot 10^{-5}$ mm/s and the maximum value of 1.75 mm/s.

4.4. Convergence of the solution for refinements of time and spatial discretisations

To gain confidence in the accuracy of the spatial and time discretisation, a convergence analysis was conducted for both of them, revealing that the solution is very close to convergence because negligible variations were observed by reducing the mesh or the time increment.

For the applied speeds of 0.01 and 100 mm/min, Figure 15 shows the curves obtained when the time increment Δt_{GL}, set equal to the maximum allowed time increment for the Newton–Raphson nonlinear solution procedure, was reduced from 0.5 s to the values of 0.2 and 0.1 s for the applied speed of 100 mm/min and from 5000 s to the values of 2000 and 1000 s for the applied speed of 0.01 mm/min. The difference in the results is so small that it cannot be appreciated in the plots.

Figures 16 shows the load-displacement curve, as well as the interface stress against time at the initial crack tip, for the mesh used in the simulations reported in Section 4.3 and for two more refined meshes in the case of an applied speed of 100 mm/min. Again the difference in results cannot be appreciated.

4.5. Sensitivity analysis

In this section, the results of a sensitivity analysis with respect to the model parameters are reported. To this end, several analyses have been conducted by modifying one parameter only in each analysis, leaving the other parameters equal to those in Table I.
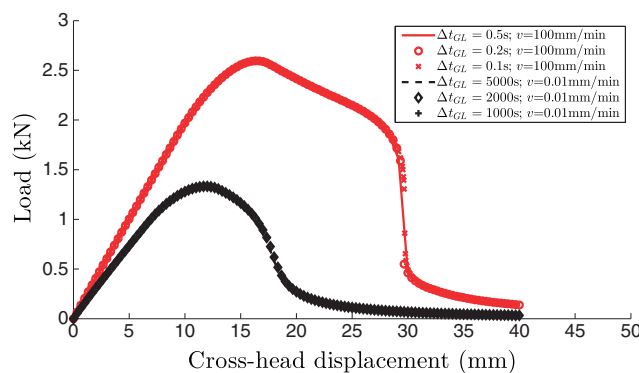

Figure 15. Influence of the time increment Δt_{GL} on the solution for the prescribed speed of 0.01 and 100 mm/min.
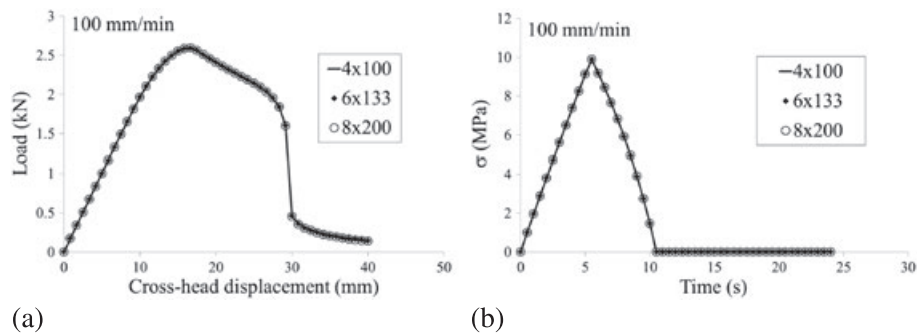
Figure 16. Influence of the mesh refinement on (a) the load-displacement curve and (b) the interface stress for a prescribed speed of 100 mm/min.
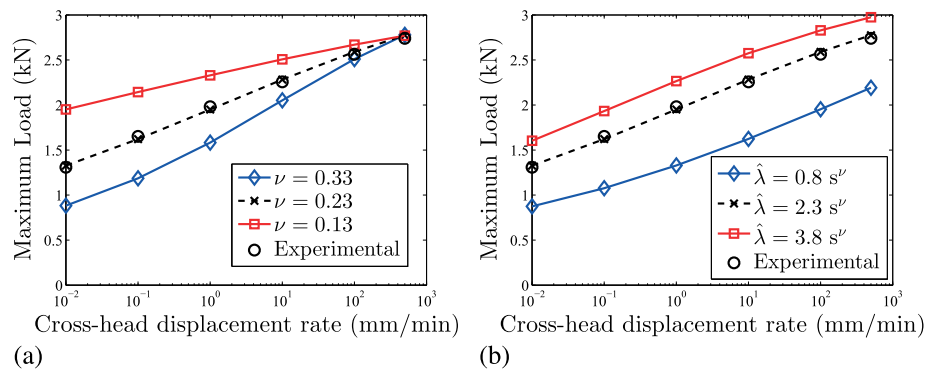

Figure 17. Influence of (a) ν and (b) $\hat{\lambda}$ on the numerically predicted load maxima.

Figures 17(a) and (b) report the load maxima plotted against the applied speeds obtained by changing either the fractional exponent ν or $\hat{\lambda}$. It can be noticed that the slope of this curve tends to increase with increasing values of ν. Instead, for increasing $\hat{\lambda}$ all points translate upwards but not exactly of the same amount as it can be appreciated that the right-hand side of the curve has increased concavity, because the fast limit is approached at the higher applied speeds. Vice versa, for decreasing $\hat{\lambda}$ all points translate downwards, but now the left-hand side of the curve has increased convexity because the slow-limit is approached at the lower applied speeds.

It is worth noting that, because $\hat{\lambda}$ has units of s^ν, it cannot be interpreted as a characteristic relaxation time. Instead, $\hat{\lambda}^{1/\nu}$ has dimensions of a time, which explains that changing ν has also the effect of scaling the time, which explains why, in Figure 17(a), changing ν also has the effect of changing the convexity or concavity of the curve. In fact, for a value of $\nu = 0.33$, both the concavity on the right-hand side and the convexity on the left-hand side can be better appreciated, suggesting that both the slow limit for the lower speeds and the fast limit for the higher speeds can be felt. In other words, for increasing values of ν, the range of speeds where the relationship between load maxima and applied speeds is nearly linear becomes smaller.

Figure 18 shows that the influence of ν on the numerically predicted load-displacement curve is higher for the applied speed of 0.01 mm/min than for the applied speed of 100 mm/min, which is in accordance with the results of Figure 17(a). Figure 19 confirms that the numerically predicted load-displacement curve is quite sensitive to the value of $\hat{\lambda}$ for both the considered applied speeds of 100 and 0.01 mm/min.

Figure 20 shows the opposite effect of changing G_{c1} and μ. Increasing G_{c1} means increasing the slow-limit total fracture energy, with a corresponding increase in the fast-limit total fracture energy G_{c1}/μ, which leads to an increase of all load maxima. Instead, increasing μ has obviously the opposite effect. This behaviour is confirmed by Figures 21 and 22, which show the influence of G_{c1} and μ on the load-displacement curve for prescribed speeds of 100 and 0.01 mm/min.
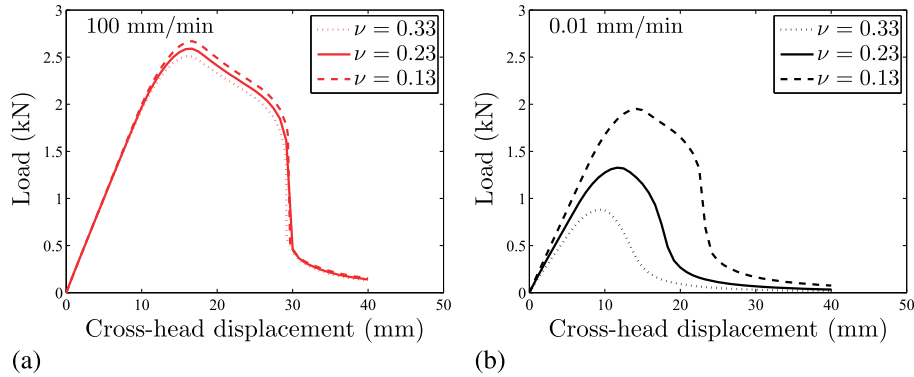
Figure 18. Influence of ν on the numerically predicted load-displacement curve for prescribed speeds of (a) 100 mm/min and (b) 0.01 mm/min.
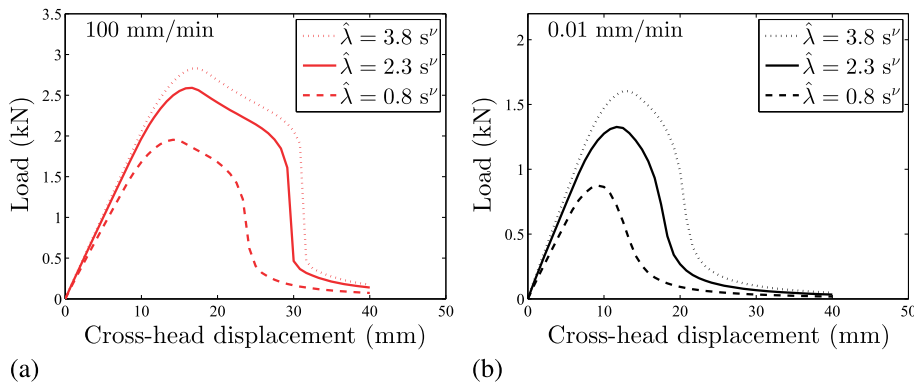

Figure 19. Influence of $\hat{\lambda}$ on the numerically predicted load-displacement curve for prescribed speeds of (a) 100 mm/min and (b) 0.01 mm/min.
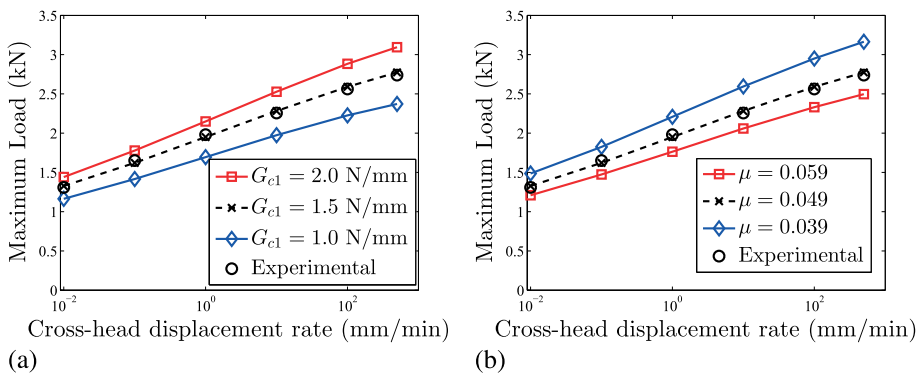

Figure 20. Influence of (a) G_{c1} and (b) μ on the numerically predicted load maxima.

Figure 23 shows that the load maxima are more sensitive to the interface strength than to the ductility β. Figure 24 shows that σ_0 has a negligible effect on the curve during the approximately self-similar crack propagation, although for $\sigma_0 = 0.5$ MPa, there is practically no self-similar propagation for both considered speeds and particularly for the lowest applied speed of 0.01 mm/min. Instead, the effect of σ_0 is non-negligible on the maximum load because the lower the σ_0, the more rounded is the curve around its peak, which is an effect already recognised for cases where the process zone is relatively large [68].
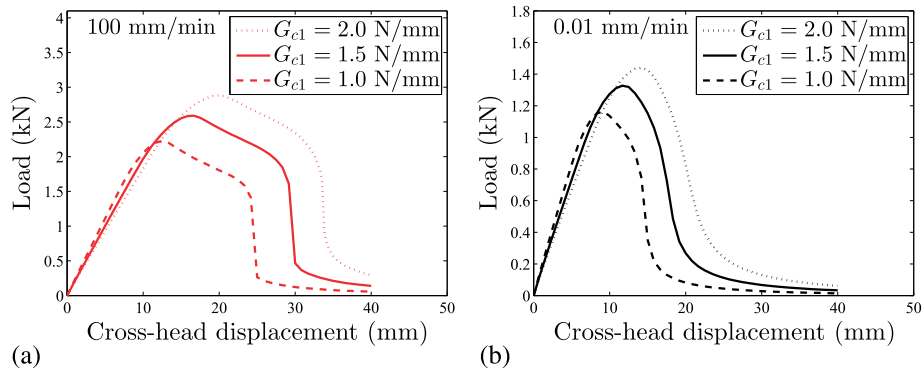
Figure 21. Influence of G_{c1} on the numerically predicted load-displacement curve for prescribed speeds of (a) 100 mm/min and (b) 0.01 mm/min.
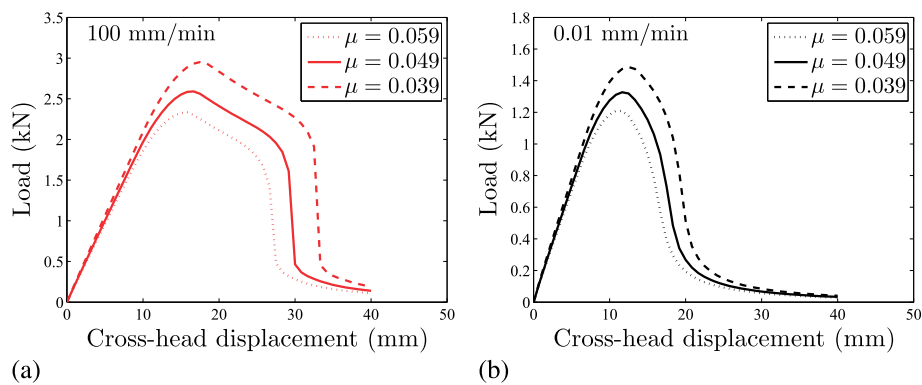

Figure 22. Influence of μ on the numerically predicted load-displacement curve for prescribed speeds of (a) 100 mm/min and (b) 0.01 mm/min.
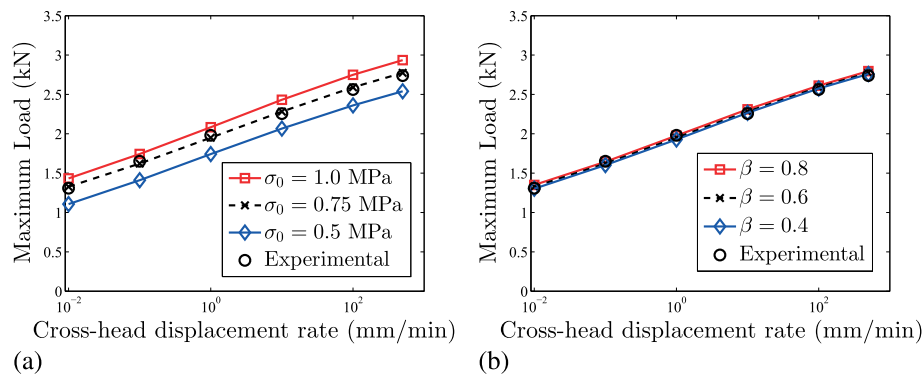

Figure 23. Influence of (a) σ_0 and (b) β on the numerically predicted load maxima.

From Figure 25, it can be appreciated that the effect of the ductility parameter β on the load-displacement curves is marked for the increasing part of the curve. This can be explained because increasing β results in increasing the stiffness of the undamaged interface, both in the slow and the fast limit, as evident from Equations (30)$_1$ and (31). Instead, the effect of β on the curves is negligible around their maximum value and during nearly self-similar crack propagation, which explains the negligible influence on the load maxima.

Finally, Figure 26 shows that the results are insensitive to relatively small values of the compressive stiffness K_c, in terms of both load maxima and load-displacement curve. Only the curve for the applied speed of 100 mm/min is reported but the same result is found also for the other applied speeds.
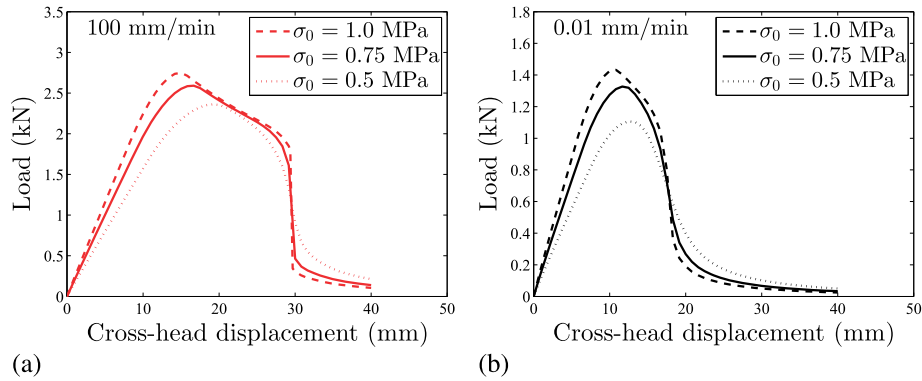
Figure 24. Influence of σ_0 on the numerically predicted load-displacement curve for prescribed speeds of (a) 100 mm/min and (b) 0.01 mm/min.
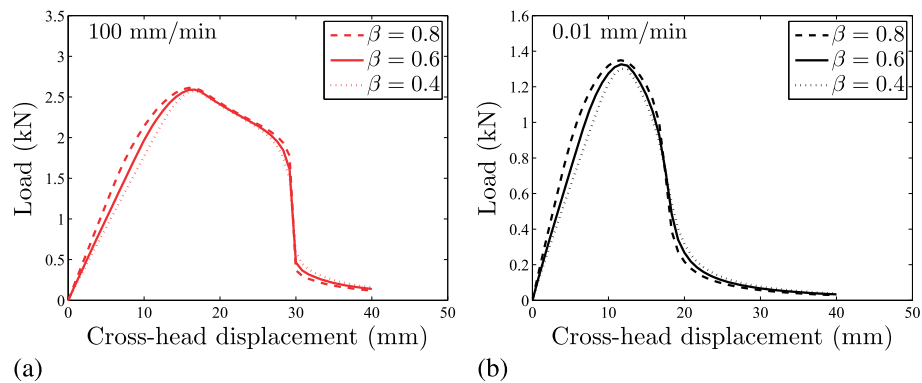

Figure 25. Influence of β on the numerically predicted load-displacement curve for prescribed speeds of (a) 100 mm/min and (b) 0.01 mm/min.
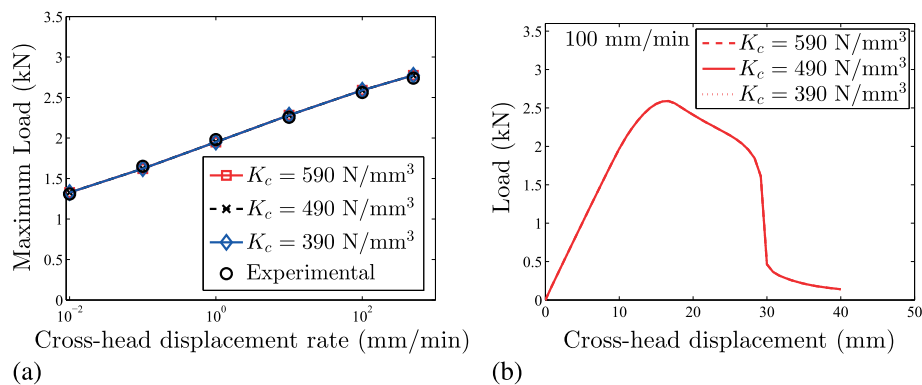

Figure 26. Influence of K_c on the numerically predicted (a) load maxima and (b) load-displacement curve for a prescribed speeds of 100 mm/min.

5. CONCLUSIONS

A new rate-dependent mode-I CZM combining damage-mechanics with fractional viscoelasticity has been presented in this paper. The model was experimentally validated with success, obtaining excellent agreement between numerical and experimental results over a range of applied speeds of almost 5 logarithmic decades, and with a single set of seven input parameters only, for the case of a DCB made of two steel arms bonded along a rubber interface.

The model starts from the main assumptions that an intrinsic, rate-independent value of the fracture energy G_{c1} exists, corresponding to the energy dissipated per unit crack area in the slow limit, and that damage is driven by the elastic energy in accordance with a rate-independent evolution law. Instead, rate dependence of the total fracture energy G_{ct} is retrieved by introducing an additional internal variable α associated with rate-dependent dissipation. The evolution of α is related to its static driving force via a fractional-order differential equation. This is equivalent, for the undamaged material, to the use of a power-law relaxation function, which much better fits the real behaviour of many polymers and, specifically, of the rubber compound considered for the validation case study in this paper.

The numerical solution of the fractional-order differential equation was based on the Grünwald-Letnikov definition of fractional derivative whose numerical approximation was calculated using a time interval Δt_{GL} to sample the history of relative displacement and stress at each point of the interface.

A convergence analysis was made and showed that, upon either reducing the chosen maximum time increment Δt_n used for the Newton-Raphson solution procedure or refining the spatial discretisation, negligible changes are obtained in the solution. Because the maximum Δt_n was set equal to Δt_{GL}, this also implies that sufficient accuracy was obtained for the approximation of the fractional derivatives.

Future work should aim at widening the experimental validation, optimising the computational cost and extending the formulation to account for large strains and mixed-mode crack propagation. The first aspect will require testing at very high speeds, which will also require accounting in the numerical simulation for dynamic effects both in the sample and possibly in the test rig, and at very slow speeds, which can be extremely time consuming unless time–temperature superposition is used. However, in the authors' opinion, on top of possible experimental inaccuracy added by the procedure, extreme care has to be taken in treating fracture and viscoelastic behaviour simultaneously using time–temperature superposition, as it seems plausible that fracture related phenomena and viscoelastic deformation scale differently with temperature due to the complex and different phenomena involved. Furthermore, the applicability of the presented model to a wider range of interface materials, including other elastomers and rate-dependent polymers, will require further investigation and validation exercises.

The minimisation of the computational cost of the calculation of fractional derivatives was outside the scope of this work, but it is expected that, following [63], this can be achieved by using a non-constant sampling time interval Δt_{GL} and by possibly neglecting part of the initial time history invoking the concept of 'fading memory', whereby events more distant in the past bear less consequences to the current response than events closer in the past.

The extension of our model to account for finite strains, which could be based on the finite-strain viscoelastic models proposed in [69] or [70], and for mixed-mode crack propagation is extremely important for many practical applications. These two aspects could be addressed separately but it is worth noting that, if the decohesion process is accompanied by significant fibrillation, it was shown in [71, 72] that fibrils bridge the crack and, even in mixed mode, they behave as nonlinear springs which can be treated as in pure mode I. In fact, the influence of fibrillation may also have implications in terms of energy dissipation (see for example [73], where the problem is studied using multi-scale computational homogenisation, or [29], where a toy model is used to explain the possible non-monotonicity of the fracture energy with respect to crack speed in presence of macroscopic fibrillation). Therefore, whether the micro-mechanics of fibrillation can be incorporated within the constitutive framework presented in this paper or, instead, some additional dissipation mechanism is to be introduced to this end, is also an important aspect which deserves investigation.

A final open issue that is left for interesting future research is whether the presented model can be derived via a consistent energetic formulation within the theory of thermodynamics with internal variables. In the first place, this requires addressing the lack of uniqueness of the free energy for fractional viscoelastic models. One could wonder whether, with the aim of determining the actual free energy of the material through reverse engineering, the fundamental ideas behind our proposed CZM could not be a point of departure.

REFERENCES

1. Xu C, Siegmund T, Ramani K. Rate-dependent crack growth in adhesives II. Experiments and analysis. *International Journal of Adhesion and Adhesives* 2003; **23**(1):15–22.
2. Karac A, Blackman BRK, Cooper V, Kinloch AJ, Rodriguez Sanchez S, Teo WS, Ivankovic A. Modelling the fracture behaviour of adhesively-bonded joints as a function of test rate. *Engineering Fracture Mechanics* 2011; **78**(6): 973–989.
3. Chan RW, Siegmund T. Vocal fold tissue failure: preliminary data and constitutive modeling. *Journal of Biomechanical Engineering - Transaction of ASME* 2004; **126**(4):466–474.
4. Oldfield M, Dini D, Giordano G, Rodriguez y Baena F. Detailed finite element modelling of deep needle insertions into a soft tissue phantom using a cohesive approach. *Computer Methods in Applied Biomechanis and Biomedical Engineering* 2013; **16**(5):530–543.
5. Persson BNJ, Brener EA. Crack propagation in viscoelastic solids. *Physical Review E* 2005; **71**:036123.
6. Schapery RA. A theory of crack initiation and growth in viscoelastic media. I. Theoretical development. *International Journal of Fracture* 1975; **11**(1):141–159.
7. Frassine R, Rink M, Leggio A, Pavan A. Experimental analysis of viscoelastic criteria for crack initiation and growth in polymers. *International Journal of Fracture* 1996; **81**:55–75.
8. Unger JF, Eckardt S, Könke C. Modelling of cohesive crack growth in concrete structures with the extended finite element method. *Computer Methods in Applied Mechanics and Engineering* 2007; **196**(41–44):4087–4100.
9. Benvenuti E. A regularized XFEM framework for embedded cohesive interfaces. *Computer Methods in Applied Mechanics and Engineering* 2008; **197**(49–50):4367–4378.
10. Verhoosel CV, de Borst R. A phase-field model for cohesive fracture. *International Journal for Numerical Methods in Engineering* 2013; **96**(1):43–62.
11. Xu C, Siegmund T, Ramani K. Rate-dependent crack growth in adhesives I. Modelling approach. *International Journal of Adhesion and Adhesives* 2003; **23**(1):9–13.
12. Corigliano A, Ricci M. Rate-dependent interface models: formulation and numerical applications. *International Journal of Solids and Structures* 2001; **38**(4):547–576.
13. Allen DH, Searcy CR. A micromechanical model for a viscoelastic cohesive zone. *International Journal of Fracture* 2001; **107**:159–176.
14. Liechti KM, Wu JD. Mixed-mode, time-dependent rubber/metal debonding. *Journal of the Mechanics and Physics of Solids* 2001; **49**(5):1039–1072.
15. Landis CM, Pardoen T, Hutchinson JW. Crack velocity dependent toughness in rate dependent materials. *Mechanics of Materials* 2000; **32**(11):663–678.
16. de Gennes PG. *Soft Interfaces: The 1994 Dirac Memorial Lecture*. Cambridge University Press: Cambridge, UK, 1997.
17. Xu DB, Hui CY, Kramer EJ. Interface fracture and viscoelastic deformation in finite size specimens. *Journal of Applied Physics* 1992; **72**(8):3305–3316.
18. Nguyen TD, Govindjee S. Numerical study of geometric constraint and cohesive parameters in steady-state viscoelastic crack growth. *International Journal of Fracture* 2006; **141**(1–2):255–268.
19. Chaboche JL, Feyel F, Monerie Y. Interface debonding models: a viscous regulatization with a limited rate dependency. *International Journal of Solids and Structures* 2001; **38**(18):3127–3160.
20. Giambanco G, Fileccia Scimemi G. Mixed mode failure analysis of bonded joints with rate-dependent interface models. *International Journal for Numerical Methods in Engineering* 2006; **67**(8):1160–1192.
21. Hauch JA, Marder MP. Energy balance in dynamic fracture, investigated by a potential drop tecnique. *International Journal of Fracture* 1998; **90**:133–151.
22. Finenberg J, Marder M. Instability in dynamic fracture. *Physics Reports* 1999; **313**:1–108.
23. Zhou F, Molinari JF, Shioya T. A rate-dependent cohesive model for simulating dynamic crack propagation in brittle materials. *Engineering Fracture Mechanics* 2005; **72**(9):1383–1410.
24. Valoroso N, Debruyne G, Laverne J. A cohesive zone model with rate-sensitivity for fast crack propagation. *Mechanics Research Communications* 2014; **58**:82–87.
25. Lake GJ, Thomas AG. The strength of highly elastic materials. *Proceedings of the Royal Society* 1967; **300**:108–119.
26. Persson BNJ, Albohr O, Heinrich G, Ueba H. Crack propagation in rubber-like materials. *Journal of Physics: Condensed Matter* 2005; **17**:R1071–R1142.
27. Kinloch AJ, Young RJ. *Fracture behaviour of polymers*. Elsevier Applied Science: London and New York, 1983.
28. Musto M, Alfano G. A novel rate-dependent cohesive-zone model combining damage and visco-elasticity. *Computers & Structures* 2013; **118**:126–133.
29. Musto M. On the formulation of hereditary cohesive-zone models. *PhD Thesis*, Brunel University London, 2014.
30. Taylor RL, Pister KS, Goudeau GL. Thermomechanical analysis of viscoelastic solids. *International Journal for Numerical Methods in Engineering* 1970; **2**(1):45–59.

31. Simo JC, Hughes TJR. *Computational Inelasticity*. Springer: Berlin, 1998.
32. Schiessel H, Blumen A. Hyerarchical analogues to fractional relaxation equations. *Journal of Physics A: Mathematical and General* 1993; **26**:5057 –5069.
33. Leibniz GW. *Mathematische Schriften*. Georg Olms Verlagsbuchhandlung, Hildesheim, 1962.
34. Mainardi F. *Fractional Calculus and Waves in Linear Viscoelasticity*. Imperial College Press, 2010.
35. Podlubny I. *Fractional differential equations*. Academic Press, 1999.
36. Heymans N, Podlubny I. Physical interpretation of initial conditions for fractional differential equations with Riemann-Liouville fractional derivatives. *Rheologica Acta* 2006; **45**:765–771.
37. Fabrizio M, Morro A. *Mathematical problems in linear viscoelasticity*. SIAM: Philadelphia, 1992.
38. Day WA. *The Thermodynamics of Simple Materials with Fading Memory*. Springer-Verlag, 1972.
39. Gurtin ME, Herrera I. On dissipation inequalities and linear viscoelasticity. *Quarterly of Applied Mathematics* 1965; **23**:235–245.
40. Akyildiz F, Jones RS, Walters K. On the spring-dashpot representation of linear viscoelastic behaviour. *Rheologica Acta* 1990; **29**:482–484.
41. Beris AN, Edwards BJ. On the admissibility criteria for linear viscoelastic kernels. *Rheologica Acta* 1993; **32**:505–510.
42. Hazanov S. New class of creep-relaxation functions. *International Journal of Solids and Structures* 1995; **32**(2):165–172.
43. Whittle Gruffudd HR. Relaxation spectrum recovery using fourier transforms. *PhD Thesis*, Pryfisgol Aberystwyth University, 2012.
44. Nutting PG. A new general law of deformation. *Journal of the Franklin Institute* 1921; **191**:679–685.
45. Scott Blair GW. The role of psychophysics in rheology. *Journal of Colloid Science* 1947; **2**(1):21–32.
46. Koeller RC. Application of fractional calculus to the theory of viscoelasticity. *Journal of Appied Mechanics* 1984; **51**:299–307.
47. Zener C. *Elasticity and anelasticity of metals*. University of Chicago Press: Chicago, 1948.
48. Jaishankar A, McKinley GH. Power-law rheology in the bulk and at the interface: quasi-properties and fractional constitutive equations. *Proceedings of the Royal Society* 2012. DOI: 10.1098/rspa.2012.0284.
49. Breuer S, Onat ET. On uniqueness in linear viscoelasticity. *Quarterly of Applied Mathematics* 1962; **19**:355–359.
50. Lion A. On the thermodynamics of fractional damping elements. *Continuum Mechanics and Thermodynamics* 1997; **9**:83–96.
51. Barenblatt GI. The mathematical theory of equilibrium cracks in brittle fracture. *Advances in Applied Mechanics* 1962; **7**:55–129.
52. Destrade M, Gilchrist MD, Motherway JA, Murphy JG. Bimodular rubber buckles early in bending. *Mechanics of Materials* 2010; **42**(4):469–476.
53. Alfano G, Crisfield MA. Finite element interface models for the delamination analysis of laminated composites: mechanical and computational issues. *International Journal for Numerical Methods in Engineering* 2001; **50**(7):1701–1736.
54. Breuer S, Onat ET. On the determination of free energy in linearly viscoelastic solids. *Zeitschrift für Angewandte Mathematik und Physik* 1964; **15**:184–191.
55. Deseri L, Di Paola M, Zingales M. Free energy and states of fractional-order hereditariness. *International Journal of Solids and Structures* 2014; **51**:3156–3167.
56. Maugin GA. *The thermomechanics of nonlinear irreversible behaviors*. World Scientific: Singapore, 1999.
57. Ortiz M, Repetto EA. Nonconvex energy minimization and dislocation structures in ductile single crystals. *Journal of the Mechanics and Physics of Solids* 1999; **47**:397 –462.
58. Miehe C, Schotte J, Lambrecht M. Homogenization of inelastic solid materials at finite strains based on incremental minimization principles. Application to the texture analysis of polycristals. *Journal of the Mechanics and Physics of Solids* 2002; **50**(10):2123–2167.
59. Oldham KB, Spanier J. *The Fractional Calculus*. Academic Press: London, 1974.
60. Grünwald AK. Über 'begrenzte' derivationen und deren anwendung. *Zeitschrift für Angewandte Mathematik und Physik* 1867; **12**:441–480.
61. Riesz M. L' integral de Riemann-Liouville et le probleme de Cauchy. *Acta Mathematica* 1949; **81**:1–122.
62. Boltzmann L. Zur Theorie der elastichen nachwirkung. *Annalen der Physik* 1878; **241**(11):430–432.
63. Schmidt A, Gaul L. Finite element formulation of viscoelastic constitutive equations using fractional time derivatives. *Nonlinear Dynamics* 2002; **29**:37–55.
64. Padovan J. Computational algorithms for FE formulations involving fractional operators. *Computational Mechanics* 1987; **2**:271–287.
65. Mi Y, Crisfield MA, Hellweg HB, Davies GAO. Progressive delamination using interface elements. *Journal of Composite Materials* 1998; **32**(14):1246–1272.
66. Corigliano A. Formulation, identification and use of interface models in the numerical analysis of composite delamination. *International Journal of Solids and Structures* 1993; **30**(20):2779–2811.
67. Corigliano A, Mariani S. Parameter identification of a time-dependent elastic-damage interface model for the simulation of debonding in composites. *Composite Science and Technology* 2001; **61**(2):191–203.
68. Alfano G. On the influence of the shape of the interface law on the application of cohesive-zone models. *Composites Science and Technology* 2006; **66**(6):723–730.
69. Drozdov AD. Fractional differential models in finite viscoelasticity. *Acta Mechanica* 1997; **124**:155–180.

70. Adolfsson K. Nonlinear fractional order viscoelasticity at large strains. *Nonlinear Dynamics* 2004; **38**:233–246.
71. van den Bosch MJ, Schreurs PJG, Geers MGD. On the development of a 3D cohesive zone element in the presence of large deformations. *Computational Mechanics* 2008; **42**:171–180.
72. van den Bosch MJ, Schreurs PJG, Geers MGD. Identification and characterization of delamination in polymer coated metal sheet. *Journal of the Mechanics and Physics of Solids* 2008; **56**(11):3259–3276.
73. Vossen BG, Schreurs PJG, van der Sluis O, Geers MGD. Multi-scale modeling of delamination through fibrillation. *Journal of the Mechanics and Physics of Solids* 2014; **66**:117–132.